

Evolving Sahel Rainfall Response to Anthropogenic Aerosols Driven by Shifting Regional Oceanic and Emission Influences

HARUKI HIRASAWA,^a PAUL J. KUSHNER,^a MICHAEL SIGMOND,^b JOHN FYFE,^b AND CLARA DESER^c

^a *Department of Physics, University of Toronto, Toronto, Ontario, Canada*

^b *Canadian Centre for Climate Change Modelling and Analysis, Environment and Climate Change Canada, Victoria, British Columbia, Canada*

^c *National Center for Atmospheric Research, Boulder, Colorado*

(Manuscript received 12 October 2021, in final form 13 January 2022)

ABSTRACT: Sahel summertime precipitation declined from the 1950s to 1970s and recovered from the 1970s to 2000s. Anthropogenic aerosol contributions to this evolution are typically attributed to interhemispheric gradient changes of Atlantic Ocean sea surface temperature (SST). However recent work by Hirasawa et al. indicates a more complex picture, with the response being a combination of “fast” direct atmospheric (DA) processes and “slow” ocean-mediated (OM) processes. Here, we extend this understanding using the Community Atmosphere Model 5 to determine the role of regional ocean-basin perturbations and regional aerosol emission changes in the overall aerosol-driven OM and DA responses, respectively. From the 1950s to 1970s, there was an OM Sahel wetting response due to Pacific Ocean cooling that was offset by drying due to Atlantic cooling. By contrast, from the 1970s to 2000s, Atlantic trends reversed and amplified the Pacific cooling-induced wetting. This wetting was partially offset by drying driven by Indian Ocean cooling. Thus, the OM Sahel precipitation response to aerosol crucially depends on the balance of responses to Atlantic, Pacific, and Indian Ocean SST anomalies. From the 1950s to 1970s, there is DA Sahel drying that was principally due to North American aerosol emissions, with negligible effect from European emissions. DA drying from the 1970s to 2000s was mainly due to African aerosol emissions. Thus, the shifting roles of regional OM and DA effects reveal a complex interplay of direct driving and remote teleconnections in determining the time evolution of Sahel precipitation due to aerosol forcing in the late twentieth century.

SIGNIFICANCE STATEMENT: Studies of global climate models consistently indicate that anthropogenic aerosol emissions were a significant contributor to a severe drought that occurred in the Sahel region of Africa in the late twentieth century. The drying influence of aerosol forcing is the combined result of rapid atmospheric responses directly due to the forcing and slower responses due to forced ocean temperature changes. Using a set of simulations targeted at determining the influences from different ocean basins and different emission regions for two periods in the late twentieth century, we find there is a surprising range of mechanisms through which aerosol emissions affect the Sahel. This results in a complex interplay of at times competing and at times complementary regional influences.

KEYWORDS: Atmosphere; Africa; Atmosphere–ocean interaction; Monsoons; Aerosols; Regional effects; General circulation models

1. Introduction

The influence of external forcing on climate variability in the Sahel region of Africa has been extensively studied, with much attention focused on understanding the drivers of the drought that afflicted the region with its peak in the 1970s and 1980s. Much of the variability is understood to be linked to global sea surface temperature (SST) variability, which is in large part internal (Folland et al. 1986; Rodríguez-Fonseca

et al. 2011; Biasutti et al. 2008; Biasutti 2019). However, an array of studies using coupled global climate model (GCM) simulations have identified anthropogenic sulfate aerosol forcing as a significant driver of drought in the Sahel (Rotstayn and Lohmann 2002; Held et al. 2005; Kawase et al. 2010; Ackerley et al. 2011; Westervelt et al. 2017; Undorf et al. 2018; Hua et al. 2019; Giannini and Kaplan 2019; Herman et al. 2020). Aerosol and their precursor emissions have undergone substantial and spatially varied changes on multi-decadal time scales. In particular, sulfur dioxide, the precursor chemical to sulfate aerosol, is characterized by an initial increasing trend up to the 1970s focused in North America and Europe and then a decrease in these regions after the 1970s along with strong increases in South and East Asia (Smith et al. 2011). The timing and spatial pattern of these aerosol changes result in multidecadal changes in Sahel climate that can be identified in single-forcing GCM simulations for which there is a sufficient ensemble size to filter internal variability (Hua et al. 2019; Deser et al. 2020).

 Denotes content that is immediately available upon publication as open access.

 Supplemental information related to this paper is available at the Journals Online website: <https://doi.org/10.1175/JCLI-D-21-0795.s1>.

Corresponding author: Haruki Hirasawa, hirasawa@physics.utoronto.ca

DOI: 10.1175/JCLI-D-21-0795.1

© 2022 American Meteorological Society. For information regarding reuse of this content and general copyright information, consult the [AMS Copyright Policy](#) (www.ametsoc.org/PUBSReuseLicenses).

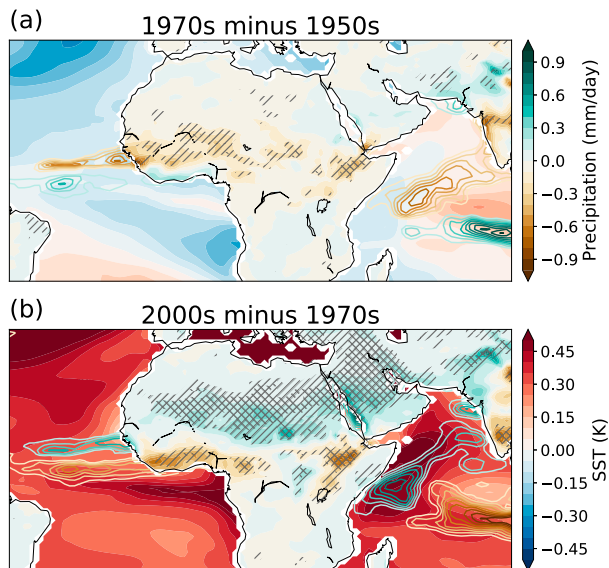


FIG. 1. JAS precipitation anomalies over land and JAS SST anomalies over ocean in filled contours from the CESM1 LE ALL-minus-XAER simulations for the (a) 1970s minus 1950s and (b) 2000s minus 1970s. Precipitation anomalies over ocean are shown using contours with the same color bar as the land precipitation but excluding the zero contour. Signals that pass a Student's *t* test at the 95% level are single hatched in gray, and signals that additionally pass the false detection rate (FDR) test are cross hatched ($p_{\text{FDR}} = 2.5 \times 10^{-3}$).

In the National Center for Atmospheric Research (NCAR) Community Earth System Model 1 (CESM1) Large Ensemble (LE) single-forcing simulations (Deser et al. 2020), it is found that aerosol forcing reduced July–September (JAS) precipitation in the Sahel for the 1970s minus 1950s (Fig. 1a) and increased precipitation for the 2000s minus 1970s (Fig. 1b). This aerosol forcing effect is the dominant driver of historical multidecadal Sahel precipitation variability in CESM1 (Hirasawa et al. 2020). GHG forcing has little contribution to the 1970s-minus-1950s change but contributes to the recovery from the 1970s onward. The CESM1 LE ensemble mean multidecadal variability in Sahel rainfall is similar in timing to the observed variability. However, both the ensemble mean and spread are substantially smaller in magnitude relative to observed variability (Hirasawa et al. 2020), which is a common problem in coupled GCMs (Biasutti 2013; Undorf et al. 2018). Such aerosol-induced impacts are typically interpreted as a response to hemispheric asymmetries in Atlantic SST anomalies caused by regional emission changes in North America and Europe. These hemispheric asymmetries drive shifts in the Atlantic intertropical convergence zone (ITCZ) and West African monsoon southward, drying the Sahel (Ackerley et al. 2011; Mohino et al. 2011; Hwang et al. 2013; Wang 2015; Hua et al. 2019). Such an interhemispheric SST anomaly pattern is also seen in the CESM1 LE aerosol forcing effect. In these simulations the sign of the interhemispheric Atlantic SST contrast anomaly switches between the 1970s-minus-1950s epoch difference (Fig. 1a over

ocean) to the 2000s-minus-1970s epoch difference (Fig. 1b over ocean). Thus, one might interpret the Sahel precipitation change seen in CESM1 as the result of this Atlantic hemispheric SST asymmetry mechanism.

However, forcing can directly cause changes in the atmosphere even in the absence of SST changes. For example, surface albedo reductions cause subsidence and thus drying in the Sahel (Charney 1975; Pausata et al. 2016; Gaetani et al. 2017). Aerosol forcing can have a similar effect, with local increases in shortwave reflectance reducing precipitation, as well as through the effect of remote aerosol changes in regions like Asia via atmospheric teleconnections (Dong et al. 2014; Dong and Sutton 2015; Liu et al. 2018; Hirasawa et al. 2020). Furthermore, independent of aerosol forcing, SST anomalies in the tropical Pacific Ocean caused by El Niño or greenhouse gas warming have substantial effects on Sahel climate by warming the tropical upper troposphere over the Sahel, which increases the threshold for convection and reduces precipitation (Rowell 2001; Giannini et al. 2008; Giannini and Kaplan 2019). Indian Ocean warming and increasing north–south SST gradients also have a drying effect on the Sahel (Chung and Ramanathan 2006; Lu 2009; Dyer et al. 2017). We therefore expect aerosol-forced cooling will have similar but opposite-sign effects to these warming effects. Thus, it is difficult to parse the pathways through which aerosol forcing influences the climate using coupled GCM experiments alone and the aerosol impact on the Sahel is influenced by a range of factors other than the North Atlantic Ocean SST change.

In our previous work (Hirasawa et al. 2020, hereinafter H2020), we used two coupled model large ensembles (CESM1 and Environment and Climate Change Canada's Canadian Earth System Model 2; CanESM2) and their respective atmosphere–land components [Canadian Atmosphere Model 4 (CanAM4) and Community Atmosphere Model 5 (CAM5) respectively] to separately identify the direct atmospheric (DA) effect of aerosol forcing due to rapid adjustments of the atmosphere and land and the slower ocean-mediated (OM) effect due to aerosol-forced SST changes. The two epochs shown in Fig. 1, the 1970s minus 1950s (early period) and the 2000s minus 1970s (late period), were examined with a suite of atmosphere–land GCM experiments. It was found that the DA effect caused JAS drying in both periods, similar to that found in Dong et al. (2014). On the other hand, the OM effect resulted in a JAS precipitation increase in the early period despite cooling of the North Atlantic relative to the South Atlantic in these experiments. In the late period, the OM effect caused additional increases in JAS Sahel precipitation. Thus, the early-period drying in the coupled model response was predominantly DA, while the late-period recovery was predominantly OM in these models. Although there were differences in the pattern and magnitude of the response, the relative roles of the DA and OM effects were qualitatively similar in the CanAM4 and CAM5.

This work seeks to extend the analysis of H2020 so as to understand the mechanisms underlying the OM and DA effects documented therein. Focusing on the NCAR CAM5

model, we use additional simulations to decompose the OM and DA effects into their regional components by applying SST anomalies in different ocean basins individually for the OM effect and emission changes in different regions individually for the DA effect. In the case of the OM effect, the basin-level decomposition was motivated by the wetting response seen in the early period, which was hypothesized to be a result of the effect of North Atlantic cooling being offset by a reverse “upped ante” effect due to tropical SST cooling (Chou and Neelin 2004; Giannini et al. 2013; Giannini and Kaplan 2019). In the case of the DA effect, the regional emission decomposition was motivated by the persistence of a DA drying signal in the late period, despite large declines in sulfate concentrations over North Africa due to declining European emissions. This drying signal was hypothesized to be a teleconnected response to increasing Asian emissions (Dong et al. 2014; Liu et al. 2018).

The experiments used here are similar to those conducted for the Precipitation Driver Response Model Intercomparison Project (PDRMIP) in which large, idealized aerosol perturbations are applied regionally to coupled GCM and AGCMs (Myhre et al. 2017; Liu et al. 2018). Liu et al. (2018) found that a large increase in Asian sulfate (black carbon) emissions caused annual-mean wetting (drying) in the Sahel that is in largely DA driven, while an increase in European sulfate emissions causes principally OM-driven drying. In this work, we instead study the decomposition of DA and OM effects for two periods characterizing first the general rise in emissions focused in North America and Europe and then the west-to-east geographic shift of aerosol emissions. The differing impact of historical aerosol forcing in these two periods has gained increasing interest in recent studies, as the short atmospheric lifetime of aerosols results in differing patterns of aerosol forcing and climate response (Wang 2015; Deser et al. 2020; Kang et al. 2021). Furthermore, we explicitly determine the OM effect by conducting AGCM experiments using aerosol-forced SST perturbations derived from a large ensemble of coupled GCM simulations, rather than as the residual between the coupled GCM and AGCM simulations as in PDRMIP (Liu et al. 2018).

In section 2, we describe the CESM1 LE and CAM5 simulations used in this analysis. In sections 3 and 4, we discuss the effect of regional SST and regional emission perturbations on the Sahel, respectively, and discuss the mechanisms underlying these responses. In section 5, we discuss the additivity of response to regional SST and regional emission perturbations. In section 6, we summarize our results and make concluding remarks.

2. Methods

The roles of the OM and DA effects on the Sahel are determined using a set of prescribed-SST simulations conducted with the NCAR–Department of Energy Community Atmosphere Model, version 5 (CAM5; Neale et al. 2012). CAM5 includes basic chemistry and represents aerosols using a three-mode aerosol model (MAM3) (Liu et al. 2012). Thus, aerosols are prescribed via specification of emissions of

aerosols and aerosol precursor chemicals. Furthermore, CAM5 includes representation of aerosol–cloud interactions including the cloud albedo and lifetime effects (Neale et al. 2012). These result in a total effective radiative forcing of -1.37 W m^{-2} by the early twenty-first century, which is relatively strong among CMIP5 models (Zelinka et al. 2014). CAM5 overestimates the enhancement of cloud liquid water path in response to aerosol perturbations from tropospheric volcanic aerosols, which may result in an overestimation of the aerosol–cloud lifetime effect (Malavelle et al. 2017; Toll et al. 2019). The simulations are carried out at a nominal 1° resolution.

Here we use so-called time-slice simulations, which have atmospheric boundary conditions that vary seasonally but are fixed year to year. The baseline SST and sea ice concentration (SIC) climatology is the 2000–09 average of the Hadley Centre Sea Ice and Sea Surface Temperature (HadISST) dataset (Hurrell et al. 2008). Climatological atmosphere and land composition conditions are taken as the 2000–09 average, based on historical data for 2000–05 and RCP8.5 emissions for 2006–09. The OM effect is determined by perturbing the climatological SST/SIC with anomalies due to aerosol forcing for the 2000s minus the 1950s or the 2000s minus the 1970s, while keeping aerosol emissions fixed at climatological values. We do not modify sea ice thickness in these simulations. The aerosol-forced SST/SIC anomalies are calculated by taking the difference between the ensemble means of historical “all forcing” (ALL) and “all-but-aerosol” (XAER) forcing simulations from the NCAR CESM1-LE (Deser et al. 2020) (Figs. 2a,c), then computing the epoch differences. The XAER forcing LE is a 20-member initial condition ensemble in which all forcings follow their historical values except for industrial aerosols, which are held to 1920 conditions. Further simulations are conducted in which the SST/SIC perturbations are only applied in one of a set of three ocean basins: the Atlantic Ocean, Arctic Ocean, and Mediterranean Sea (ATL), the Indian and Southern Oceans (IND), and the Pacific Ocean (PAC) (colored contours in Figs. 2a and 2c).

The DA effect is determined by modifying emissions of aerosols and their precursor chemicals to the target decadal levels, while keeping SST/SIC conditions at 2000s levels [the resulting sulfate (SO_4) and black carbon (BC) burden changes are shown in Figs. 2b and 2d herein and Figs. S1a and S1b in the online supplemental material, respectively]. Further simulations are then conducted in which emissions are only changed in one of four emission regions: North America (NAM), Europe (EURO), Africa (AFRI), and Asia (ASIA), the definitions for which are shown using the dashed lines in Figs. 2b and 2d. Note that we do not include all possible emission regions and have not tested regions such as the Arabian Peninsula, South America, and Oceania. Nevertheless, the selected emission regions account for the vast majority of SO_4 and BC burden anomalies (Fig. S2 in the online supplemental material). Over Africa, there are differences in the SO_4 burden between the global emission change and the sum of the regional experiments, particularly near the Arabian Peninsula and Europe, but these differences are not statistically significant. In both DA and OM experiments, we conduct 2000s-minus-1970s

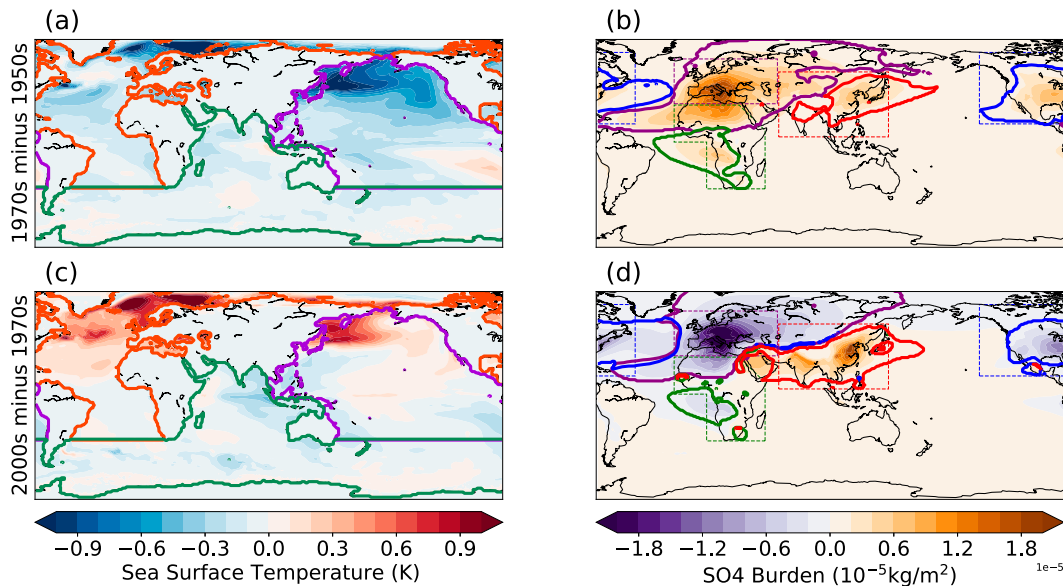


FIG. 2. For the (top) 1970s minus 1950s and (bottom) 2000s minus 1970s, (a),(c) the aerosol-forced JAS sea surface temperature (SST) anomalies from the CESM1 LE ALL-minus-XAER simulations and (b),(d) sulfate (SO_4) burden anomalies from the total direct atmospheric response simulations. In (a) and (c) the ocean basins used in the regional ocean-mediated response simulations are outlined in orange (ATL), green (IND), and purple (PAC). In (b) and (d) solid contours indicate the regions in which the SO_4 burden anomaly for a given regional emissions simulation accounts for more than 50% of the total SO_4 burden anomaly and has a magnitude greater than $10^{-6} \text{ kg m}^{-2}$. The geographic regions used to define the emissions from a given region are outlined using dashed lines in blue (N AM), purple (EURO), green (AFRI), and red (ASIA). Note that we apply the 2000s-minus-1970s and 2000s-minus-1950s anomalies in the simulations but show the 1970s-minus-1950s anomaly for easier comparison with our results. JAS anomalies are shown for direct comparison of the forcings with the responses in later figures.

and 2000s-minus-1950s experiments, with the 1970s-minus-1950s response calculated as the difference of the two. This results in more noise in the 1970s-minus-1950s responses. Descriptions of the simulations are summarized in Table 1. Each of the time-slice experiments include a minimum of 50 years of data, with some including up to 100 years.

We expect the combined DA and OM effects to closely approximate the aerosol-forced response seen in the CESM1 LE, and we find this to be the case despite possible errors due to the idealized nature of AGCM experiments (H2020). However, we found statistically significant nonlinearity in the response for the 1970s minus 1950s, which suggests a sensitivity of the OM or DA response to background aerosol or SST conditions respectively. Unlike in H2020, we only display the precipitation anomaly in the case of climatological background emission and SST conditions for the OM and DA response, respectively. Assuming additivity between the regional effects, the sum of responses in the regional OM and DA experiments should approximate the effect of the global OM and DA responses, respectively. A more detailed discussion of the additivity can be found in section 5.

In addition to evaluating the statistical significance of our results using a Student's t test, we perform false detection rate (FDR) analysis of the tests in order to identify aspects of the climate response that are more robust to internal variability. Following Wilks (2016), we select a global test threshold of 0.1, assuming high spatial correlation in seasonal average

anomalies for all variables, which corresponds to an FDR threshold of about 0.05 (i.e., approximately 5% of the tests that pass the FDR criterion are false rejections of the null hypothesis). The FDR criteria are calculated using t -test p values from all spatial grid points globally and from all experiments in the set of all OM or all DA experiments (e.g., across all regional SST perturbation experiments), treating the set of experiments as a single set of tests.

The regionally averaged response is analyzed using bootstrap resampling to estimate the uncertainty in the time mean anomalies. Making the standard assumption of statistical independence of individual years in the time-slice AGCM simulations, years in the simulations are randomly sampled with replacement, the time average taken, and the anomaly calculated. This is repeated 10^5 times to obtain a distribution that is displayed using box plots (Figs. 3i,j and 6i,j) for which the boxes represent the interquartile range, and the whiskers represent the 5th–95th-percentile range. For in-text averages mean anomalies are shown with the 5th–95th-percentile range in brackets. Thus, a given experiment is said to result in a significant increase if the lower whisker is above zero and a significant decrease if the upper whisker is below zero. By resampling the mean in each simulation for a given experiment, we estimate the effect of differencing and adding multiple experiments on the uncertainty in the mean, giving a more robust estimate of the uncertainty in the sum of regional perturbation effects.

TABLE 1. Descriptions of the SST/SIC and aerosol emission conditions in CAM5 atmosphere GCM simulations and their lengths.

Simulation	SST and SIC conditions	Aerosol emission conditions	No. of simulation years
CTRL	HadISST 2000–09 average	2000–05 historical + RCP8.5	100
<i>Ocean-mediated experiments</i>			
GLOB1970	Subtract 2000s–1970s CESM1 ALL-XAER SST anomaly globally	Same as CTRL	50
GLOB1950	Subtract 2000s–1950s CESM1 ALL-XAER SST anomaly globally	Same as CTRL	50
ATL1970	Subtract 2000s–1970s SST anomaly in Atlantic and Arctic Oceans and SIC anomaly in the NH	Same as CTRL	50
ATL1950	Subtract 2000s–1950s SST anomaly in Atlantic and Arctic Oceans and SIC anomaly in the NH	Same as CTRL	50
PAC1970	Subtract 2000s–1970s SST anomaly in the Pacific Ocean	Same as CTRL	50
PAC1950	Subtract 2000s–1950s SST anomaly in the Pacific Ocean	Same as CTRL	50
IND1970	Subtract 2000s–1970s SST anomaly in the Indian and Southern Ocean and SIC anomaly in the SH	Same as CTRL	50
IND1950	Subtract 2000s–1950s SST anomaly in the Indian and Southern Ocean and SIC anomaly in the SH	Same as CTRL	50
<i>Direct atmospheric experiments</i>			
GLOB1970	Same as CTRL	Set global emissions to 1970s levels	100
GLOB1950	Same as CTRL	Set global emissions to 1950s levels	100
NAMER1970	Same as CTRL	Set North American emissions to 1970s	50
NAMER1950	Same as CTRL	Set North American emissions to 1950s	50
ASIA1970	Same as CTRL	Set Asian emissions to 1970s	50
ASIA1950	Same as CTRL	Set Asian emissions to 1950s	50
EURO1970	Same as CTRL	Set European emissions to 1970s	50
EURO1950	Same as CTRL	Set European emissions to 1950s	50
AFRICA1970	Same as CTRL	Set African emissions to 1970s	50
AFRICA1950	Same as CTRL	Set African emissions to 1950s	50

3. Regional ocean-mediated results

The responses of African precipitation to aerosol-forced SST anomalies are shown in Fig. 3. For the 1970s minus 1950s, the global SST anomalies result in a small but significant increase in Sahel precipitation (0.18 [0.01, 0.35] mm day⁻¹; values in square brackets indicate the 5th–95th-percentile range) (Figs. 3a,i). Using the regional SST perturbation experiments, we find that this response is a result of opposing effects of Atlantic and Pacific SST anomalies (Figs. 3b–d). Cooling in the North Atlantic in this period reduces precipitation across the tropical Atlantic and the Sahel (−0.36 [−0.52, −0.21]) (Fig. 3b), as expected based on the ITCZ shift mechanism. Pacific SST cooling increases precipitation throughout the Sahel (0.36 [0.19, 0.53] mm day⁻¹), with particularly large effects in the eastern Sahel (Fig. 3c) and Indian SST cooling has little effect over the Sahel during this period (−0.05 [−0.19, 0.09]) (Fig. 3d). Thus, the net OM effect depends on the relative magnitude of Atlantic and Pacific SST effects.

For the 2000s minus 1970s, the global OM effect causes a weak and nonsignificant Sahel precipitation increase (0.06 [−0.08, 0.22] mm day⁻¹) as a result of offsetting drying in the

eastern Sahel and wetting in the western and southern Sahel (Figs. 3e,j; H2020). We find that the North Atlantic warming caused by reduced Atlantic sector aerosol emissions in this period produces a northward shift of the Atlantic ITCZ and a wetting signal in the western and central Sahel (0.23 [0.11, 0.36] mm day⁻¹) (Fig. 3f). Despite substantial warming in the midlatitude North Pacific, Pacific SST anomalies continue to cause wetting (0.17 [0.03, 0.30] mm day⁻¹), although it is now largest in the west Sahel (Fig. 3g). Indian Ocean cooling causes drying during this period that is marginally not significant in the regional average (−0.10 [−0.22, 0.03] mm day⁻¹). This is due to drying in the eastern Sahel that is partially offset by wetting in the southwest Sahel (Fig. 3h). This Indian OM signal appears to be the cause of the eastern Sahel drying in the global OM effect. We find grid points in the Sahel that pass the FDR criterion for all OM responses except the early-period Indian Ocean SST effect, indicating that these portions of the response are robust to internal variability (Figs. 3a–h).

The wetting response to Pacific SST cooling, particularly in the early period, suggests a “reverse upped-ante” type response over Africa, wherein the surface cooling in the tropical Pacific reduces diabatic heating over the region and cools

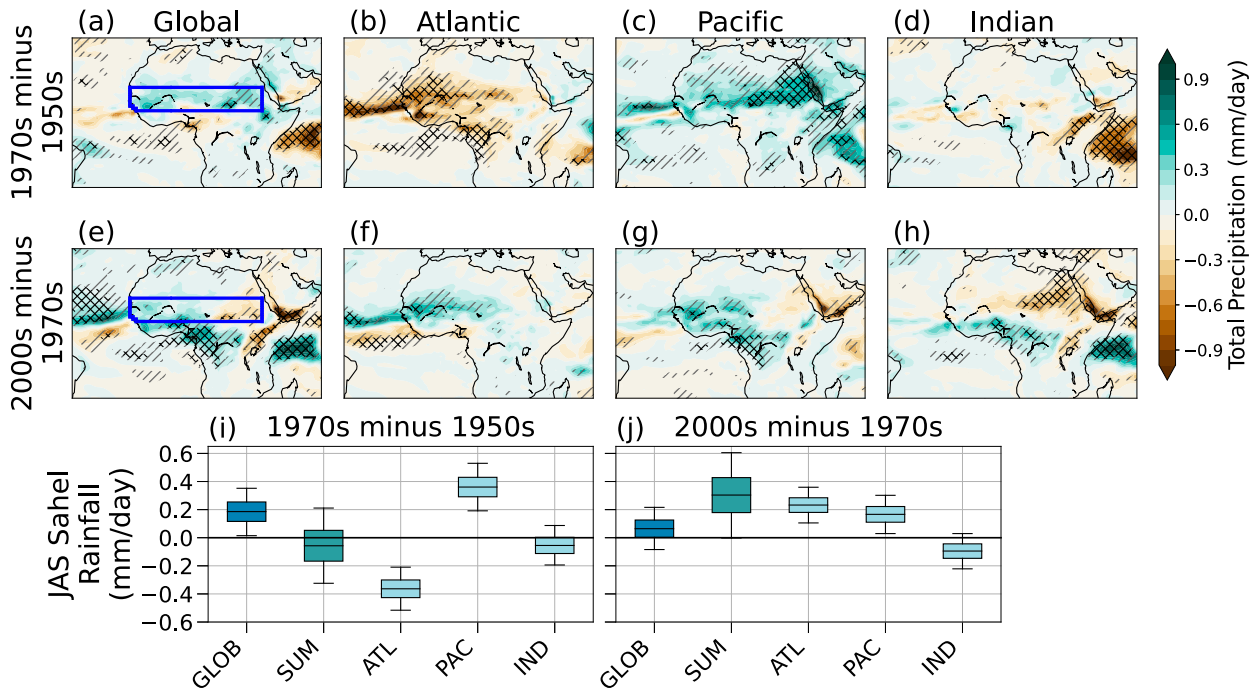


FIG. 3. JAS precipitation anomaly maps from the ocean-mediated experiments for the (top) 1970s minus 1950s and (middle) 2000s minus 1970s for the (a),(e) global, (b),(f) Atlantic, (c),(g) Pacific, and (d),(h) Indian SST anomalies. Single hatching indicates grid points that pass the t test at the 95% threshold, and cross hatching indicates points that additionally pass the FDR criterion ($p_{\text{FDR}} = 3.6 \times 10^{-3}$). The regional average anomalies [averaging region outlined in blue in (a) and (e)] are shown for the (i) 1970s minus 1950s and (j) 2000s minus 1970s following the description in section 2. The SUM box displays the sum of anomalies from the ATL, PAC, and IND experiments.

the tropical troposphere globally. As there is no corresponding cooling near the surface over Africa, this brings about a reduction in moist stability, which in turn increases convection. This effect can be seen in the early-period zonal mean

moist static energy (MSE) anomalies over Africa (Fig. 4c), where there is a MSE decrease in the upper troposphere due to cooling. This is associated with anomalous upper-level convergence over the Pacific and divergence over the Indian

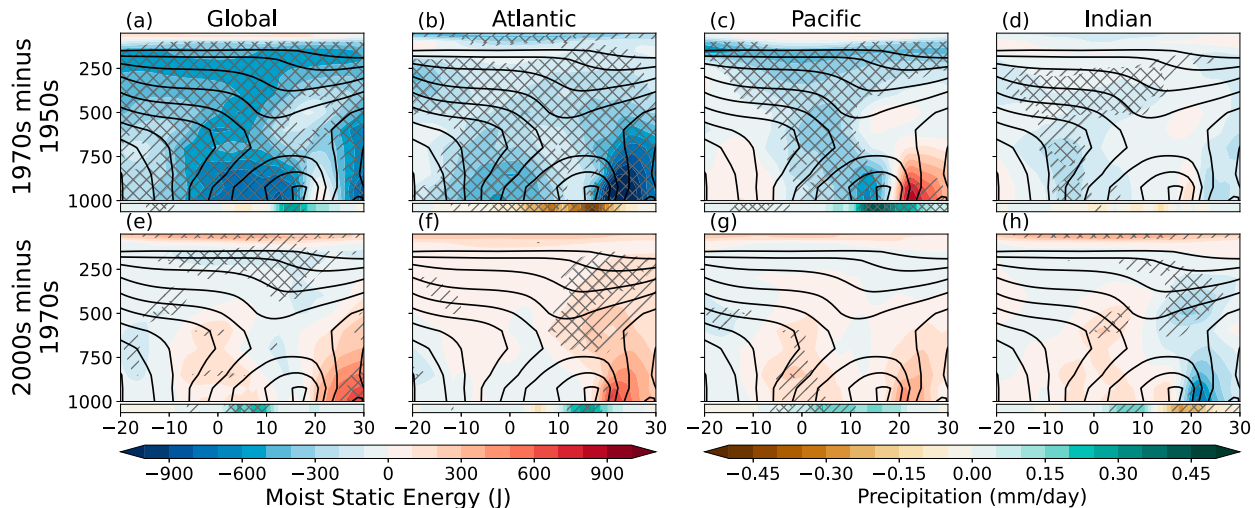


FIG. 4. JAS moist static energy (MSE) anomaly (filled contours) and climatology (black contours) zonally averaged over Africa (15°E – 35°W) of the ocean-mediated response for the (top) 1970s minus 1950s and (bottom) 2000s minus 1970s. The zonal average precipitation anomaly is plotted in the inset along the bottom of each panel. Single hatching indicates grid points where the signal passes a t test at 95% significance, and cross hatching indicates where the grid points additionally pass the FDR criterion (MSE $p_{\text{FDR}} = 0.012$; precipitation $p_{\text{FDR}} = 6.3 \times 10^{-3}$).

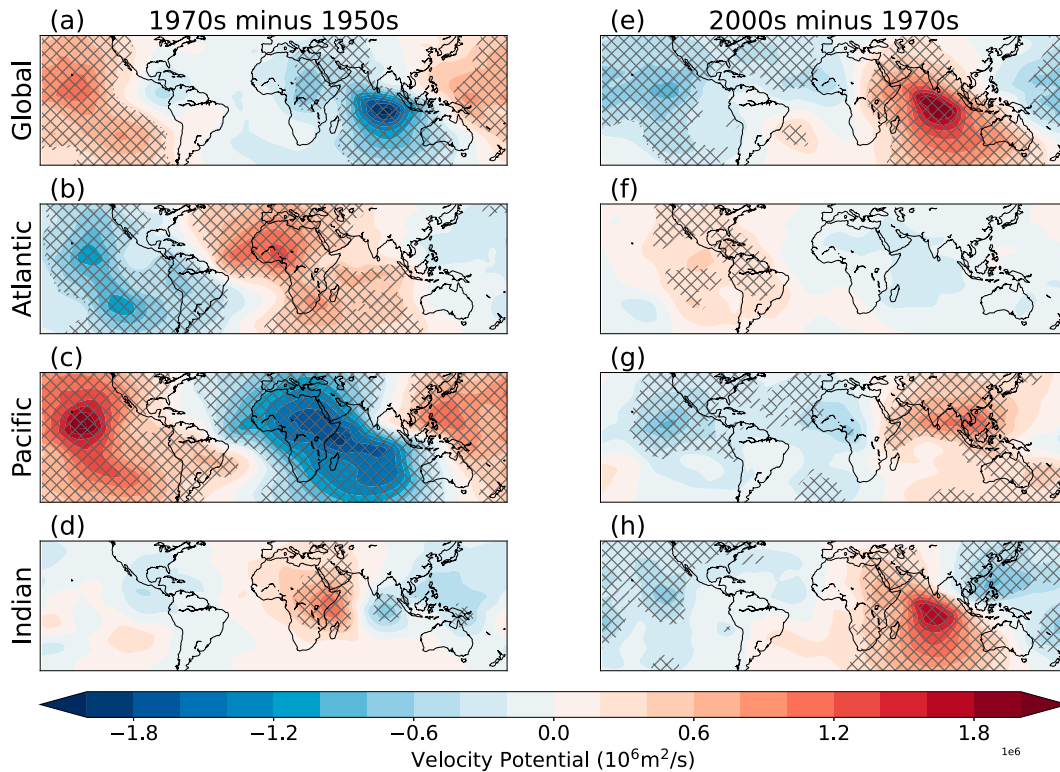


FIG. 5. JAS 200-hPa velocity potential anomaly due to ocean-mediated responses for the (left) 1970s minus 1950s and (right) 2000s minus 1970s for (a),(e) global, (b),(f) Atlantic, (c),(g) Pacific, and (d),(h) Indian SST anomaly effects. Single hatching indicates grid points where the response is significant at the 95% level via t test, with cross hatching indicating grid points where the tests additionally pass the FDR criterion ($p_{\text{FDR}} = 0.04$).

Ocean and Africa (Fig. 5c), along with streamfunction anomalies flanking the velocity potential anomalies indicating a Walker circulation change (not shown), overall resembling a Gill-type response to the Pacific SST cooling (Gill 1980; Rowell 2001). Near the surface, the local MSE maximum shifts north in response to the aerosol-forced Pacific SST changes (Fig. 4c), in agreement with the theory that the position of the MSE maximum and the northernmost limit of the monsoon circulation are collocated (Privé and Plumb 2007).

In the late period, we see continued precipitation increases due to Pacific SST anomalies (Figs. 3g,j) despite weaker and more geographically restricted SST cooling in the basin, including warming in the midlatitude North Pacific (Fig. 2c). We find there is no significant upper troposphere MSE decrease in the zonal mean for this period (Fig. 4g), although there is a weak but significant decline in 200 hPa MSE over the east Sahel (not shown). There is a Walker circulation response with upper-level convergence over the west Pacific and Indian Ocean and divergence over Africa and the east Pacific (Fig. 5g) and we posit that this is due to the continued cooling in the west Pacific, east of Asian emission regions (Fig. 2c). This cooling thus influences Africa via the Walker circulation in a mechanism similar to, but weaker than, the early-period response.

In the response to Atlantic SST anomalies, the precipitation responses follow the cooling versus warming of the subtropical

North Atlantic in the early versus late periods. The ITCZ shifts south and weakens corresponding to the cooling of the North Atlantic and conversely shifts north and strengthens corresponding to the warming of the North Atlantic, with African monsoon precipitation following the ITCZ shifts. We see the largest MSE changes over Africa occurring to the north of the climatological MSE maximum, corresponding to the southward intensification of the monsoon circulation in the early period (Fig. 4b) and a reversal of this shift in the late period (Fig. 4f). In contrast to the Pacific response, MSE anomalies for Atlantic SST change occur mainly in the lower troposphere where decreases or increases in MSE will tend to decrease or increase convection, respectively, and thus precipitation. When this is combined with the Pacific response, we see a general MSE reduction in the tropospheric column (Fig. 4a). Thus, depending on the balance of the Pacific and Atlantic Ocean influences one may find a weak or positive JAS Sahel precipitation change despite the overall cooling of the Northern Hemisphere. Our results align with the mechanism proposed by Giannini et al. (2013), in which the Sahel response to SST forcing is the result of a balance of effects from anomalies in the subtropical North Atlantic versus the global tropical ocean.

Although Indian Ocean SSTs show similar basinwide -0.10°C cooling in both periods, the early-period anomalies have little effect on Africa whereas the late-period anomalies

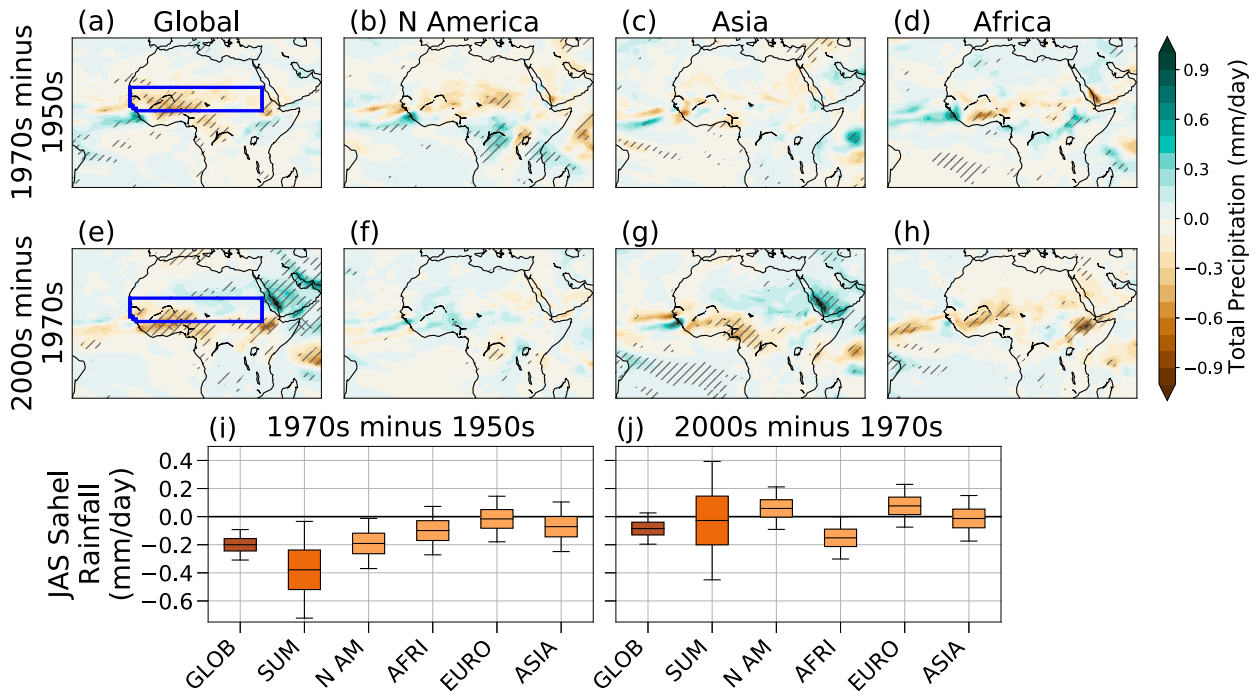


FIG. 6. JAS precipitation anomaly maps from the direct atmospheric experiments for the (top) 1970s minus 1950s and (middle) 2000s minus 1970s for the (a),(e) global, (b),(f) North American, (c),(g) Asian, and (d),(h) African emission changes. Single hatching indicates grid points that pass the t test at the 95% threshold, and cross hatching indicates points that additionally pass the FDR criterion ($p_{\text{FDR}} = 9 \times 10^{-5}$). The regional average anomalies [averaging region outlined in blue in (a) and (e)] are shown for the (i) 1970s minus 1950s and (j) 2000s minus 1970s following the description in section 2. The SUM box displays the sum of anomalies from the N AM, AFRI, EURO, and ASIA experiments.

cause significant drying in the eastern Sahel. We hypothesize this is due to the differing patterns of Indian Ocean cooling between the periods, which may be associated with emissions shifting from Europe to Asia. The early-period cooling occurs mainly in the tropical western Indian Ocean with little change in the east (Fig. 2a). This pattern weakens the summertime north–south SST gradient in the Indian Ocean and increases Sahel precipitation while the overall mean cooling signal causes drying (Chung and Ramanathan 2006; Dyer et al. 2017). This causes upper-level convergence over East Africa and divergence over the east Indian Ocean (Fig. 5d), resulting in drying over parts of East Africa but with little effect on the Sahel. For the late period, the pattern of Indian Ocean cooling differs from the previous period, with cooling being focused near the equator and in the central and eastern Indian Ocean. This results in a positive north–south gradient anomaly that, along with the overall cooling, tends to cause drying in the eastern Sahel (Chung and Ramanathan 2006; Dyer et al. 2017). This is associated with an upper-level convergence anomaly that covers much of the Indian Ocean and East Africa and divergence over the Pacific and weak divergence anomalies over the North Atlantic (Fig. 5h).

4. Regional direct atmospheric response

For the 1970s minus 1950s, global emission change causes drying in the Sahel ($-0.20 [-0.31, -0.09]$ mm day $^{-1}$) (Fig. 6a). This is the result of a combination of effects from all

emission regions as the sum of the regional emissions responses is a statistically significant drying ($-0.38 [-0.72, -0.03]$ mm day $^{-1}$), which is consistent with the global emission effect (Fig. 6i). However, only North American emission changes cause significant drying ($-0.19 [-0.37, -0.01]$ mm day $^{-1}$) (Fig. 6i), which mainly occurs in the eastern Sahel (Fig. 6b). For the 2000s minus 1970s, the global emission effect causes some nonsignificant drying in the Sahel ($-0.08 [-0.20, 0.03]$ mm day $^{-1}$), along with drying in the Gulf of Guinea region (Fig. 6e). Drying in the Sahel is mainly due to African emission increases, which cause a statistically significant drying ($-0.15 [-0.30, 0.0]$ mm day $^{-1}$) (Figs. 6h,j). Asian emission increases have little effect on the Sahel ($-0.01 [-0.17, 0.15]$ mm day $^{-1}$) but are the main cause of the drying effect in the Gulf of Guinea and central African regions (Fig. 6g). The sum of these effects is a weak anomaly in the Sahel ($-0.03 [-0.45, 0.39]$ mm day $^{-1}$) (Fig. 6j). In the spatial maps, some experiments result in precipitation responses that are significant at the 95% level in Africa; however, only late-period African emissions result in FDR significant anomalies that occur in the Ethiopian highlands (Fig. 6h). Thus, the DA precipitation responses have a lower signal-to-noise ratio than the OM responses. The DA Sahel drying effect of North American emissions in this period indicates that the CESM1 Sahel wetting signal in response to decreasing United States SO $_2$ emissions found by Westervelt et al. (2017) is not entirely driven via

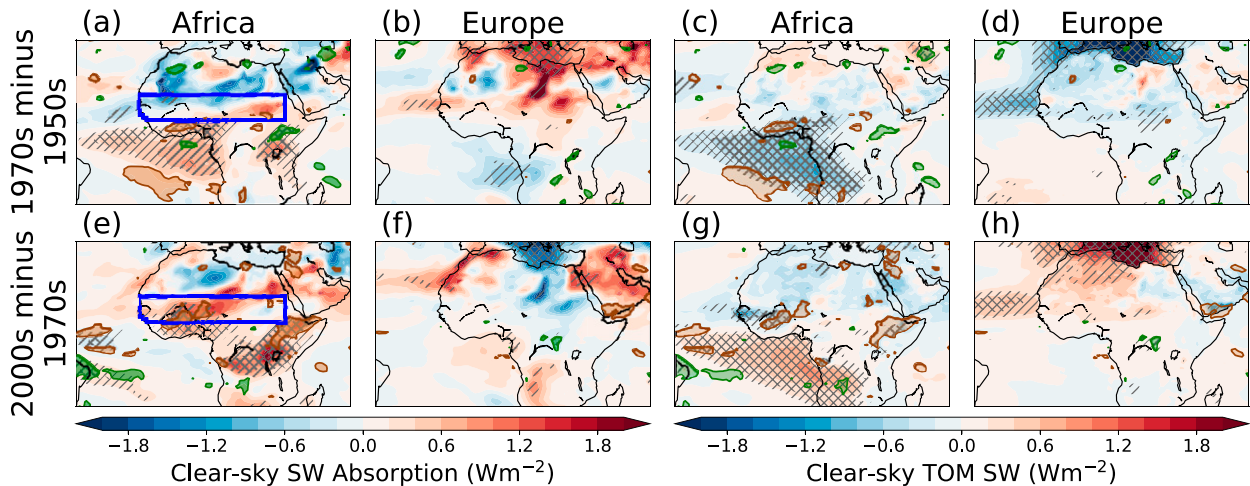


FIG. 7. (a),(b),(e),(f) Clear-sky atmospheric SW absorption shortwave anomalies and (c),(d),(g),(h) clear-sky top-of-model (TOM) anomalies for the African [1970s minus 1950s in (a) and (c); 2000s minus 1970s in (e) and (g)] and European [1970s minus 1950s in (b) and (d); 2000s minus 1970s in (f) and (h)] emission change simulations. Hatching indicates regions of statistical significance, and cross hatching indicates regions that additionally pass the FDR criterion. Grid points in which there are statistically significant ($p < 0.05$) drying (brown) or wetting (green) signals are shown in contours.

the hemispheric temperature responses but rather is also partly DA.

Despite European emissions being the primary source of sulfate burden changes in northern Africa (and the Sahel) in both periods (Figs. 1c,d, purple contours), we find that they have little effect on Sahel precipitation in either period (Figs. 6i,j). This appears to be due to weak direct aerosol radiative forcing as indicated by relatively weak anomalies in top-of-model (TOM) clear-sky net shortwave anomalies over land in North Africa in both periods (Figs. 7d,h). The weak direct forcing may be due to the high background albedo and aerosol concentrations of the Sahara, as clear-sky shortwave anomalies are stronger over the subtropical Atlantic off the coast of Africa than adjacent land regions, despite similar sulfate burden changes (Fig. 2b). This differs from the previous study by Dong et al. (2014) wherein it was found that increasing European sulfate emissions caused DA drying in the Sahel. But this result is consistent with the lack of a DA effect in CAM5 in response to a $10\times$ increase in European sulfate emissions shown in Liu et al. (2018). Thus, it appears the strength of the European sulfate emission DA drying effect is model dependent.

The largest contributor to the DA effect in the early period is North American emission changes. However, these emission changes have a minimal impact on North African aerosol burdens (Fig. 2b, along with supplemental Fig. S1a) and SW forcing (Figs. S5a,c in the online supplemental material). Thus, the DA effect of North American emissions appears to be a remote circulation response, mediated through circulation changes over the North Atlantic (Figs. S4a,e in the online supplemental material). African emissions also cause drying, although this mainly occurs in coastal regions of West Africa. This is the result of SW forcing in the coastal and tropical regions of Africa (Figs. 7a,c).

In the late period, the two main DA influences on West Africa come from Asian emissions, which cause drying in coastal West Africa, and from African emissions, which cause drying in the west Sahel. The Asian emission response seen here is consistent with the DA drying signal found in Dong et al. (2014) and disagrees with the multimodel mean DA sulfate effect of Liu et al. (2018), but has a similar pattern of response to the CAM5 experiment shown therein. Thus, it appears that the Asian DA effect is predominantly driven by sulfate cooling of Asian land regions, which shifts Asian monsoon circulation, causing anomalous upper-level divergence (Fig. 5d) and upper-tropospheric warming over the Indian Ocean. This warming signal spreads over the tropical upper troposphere, inducing a Walker circulation adjustment with upper-level convergence (Fig. S4d in the online supplemental material) and drying effects over West Africa. Local African emissions result in increases in black carbon burden across Africa and sulfate burden over West Sahel in this period (Fig. 2d; see also supplemental Fig. S1b). This results in a decrease in TOM clear-sky shortwave radiation (SW) and increase in SW absorption over West Africa (Figs. 7f,h), which both contribute to the drying signal. The TOM SW forcing by radiative cooling-induced subsidence (Dong et al. 2014) and the SW absorption by warming and stabilizing the troposphere (Andrews et al. 2010; Samsset et al. 2016). The SW atmospheric absorption anomalies in West Africa are largely collocated with the precipitation response (Fig. 7e), while the strongest TOM SW anomalies occur to the west of the drying signal (Fig. 7g). This suggests that absorbing aerosols may be the principal cause of the drying effect.

5. Additivity in regional simulations

As noted in section 2, given the design of the regional SST and emission experiments, we expect the sum of the regional

SST and emission experiments responses to approximate the global OM and DA responses respectively. For the regional OM responses, we find that the sum of regional SST precipitation responses differs from the global OM effect in both periods, with the sum inducing drying ($-0.06 [-0.32, 0.21]$ mm day⁻¹) as opposed to wetting ($0.18 [0.01, 0.35]$ mm day⁻¹) in the early period (Figs. S3c,d in the online supplemental material) and a much stronger wetting ($0.31 [0, 0.61]$ mm day⁻¹) than the global SST effect ($0.06 [-0.08, 0.22]$ mm day⁻¹) in the later period (Figs. S3g,h). However, while the differences are substantial, they are statistically nonsignificant due to the high level of noise introduced by adding together experiments (Figs. S3d,h). This is more clearly demonstrated by the sum box plots in Figs. 3i and 3j wherein we find the mean global OM response in the Sahel falls within the 5th–95th percentile range of bootstrap resampled sum responses in both periods, despite opposite-signed mean responses in the early period. Thus, it is not possible to ascertain whether there are significant nonlinearities in the response. However, analysis of the 200-hPa velocity potential, which has greater signal to noise, shows similar patterns of response in the sum and global OM responses with no significant nonadditivity (Fig. S6 in the online supplemental material). Key features are captured such as the cancellation of early-period Atlantic and Pacific OM responses over the Atlantic and Africa (Fig. S6c), which corresponds to the weak global OM velocity potential response over those regions (Fig. S6a). Similar additivity across the OM simulations is also seen in the zonally averaged MSE response over Africa (not shown), suggesting that large-scale atmospheric responses to OM can be reasonably attributed to responses from different ocean basins.

In the regional emission and global DA response case, we again find differences in precipitation response between the sum of regional emission experiments and the global DA response (Figs. S3a,e in the online supplemental material), although the agreement in sign and pattern is better in comparison with the sum of OM responses. In both periods, the spread of mean values in the global emission simulations lies entirely within the wide spread of the uncertainty in the regional sum (Figs. 6i,j). Thus, we cannot ascertain if the emissions regions we have not tested have an important role in explaining the residual or if there are nonlinear effects. In comparing the 200-hPa velocity potential responses, we find less agreement than in the OM sum case, with differences in both periods, particularly over the Pacific (Fig. S7 in the online supplemental material). However, these velocity potential responses have lower a signal-to-noise ratio than the OM responses. Nevertheless, the sign of the response is consistent over Africa. Thus, while there are apparent differences between the sum of regional effects and the global effect for both OM and DA and for both periods, the noise introduced by the summation renders it difficult to determine if these are statistically significant nonadditive signals, particularly for noisy variables such as precipitation.

6. Conclusions

In our previous work (H2020) we found that for the 1970s minus 1950s the OM component of the Sahel response to

aerosol forcing resulted in a weak increase in precipitation with the DA component causing most of the drying. For the 2000s minus 1970s, we found that the OM effect increases Sahel precipitation while the DA effect continues to cause drying. However, these simulations were not able to resolve the question of why OM response resulted in increased Sahel precipitation despite substantial cooling in the North Atlantic for the early period, and why the DA response continued to cause drying despite large declines in sulfate burdens over North Africa for the late period. To address these questions, we have regionally decomposed the DA and OM effects in CAM5. Using time-slice AGCM simulations, we identified the regional OM response by applying aerosol-induced SST anomalies in different basins and the regional DA response by changing aerosol emissions in different regions. In doing so, we gain insight into the mechanisms driving the aerosol-forced influence on Sahel climate and find that the pattern of SST and emission change is crucial for dictating the overall response.

We find that the aerosol-forced OM response is principally determined by the balance of Atlantic and tropical Pacific SST anomaly effects, with additional modulating effects due to Indian Ocean anomalies. Due to changing European and North American emissions, North Atlantic SST anomalies switch sign between the early and late periods, changing the Atlantic SST effect from Sahel drying to wetting. Pacific SST also undergo multidecadal variations, but there is cooling in the tropical west Pacific in both periods, which drives Sahel wetting. Thus, the two basins have opposing effects in the early period, with the Pacific-induced wetting overwhelming the North Atlantic-induced drying, and complementary effects in the later period, causing wetting. Indian Ocean cooling has little effect in the early period but causes drying in the late period, possibly because of a change in the sign of the north–south gradient in SST anomalies.

The aerosol DA drying in the Sahel is the result of emissions from different regions in the two periods. Early-period drying is predominantly due to North American emissions, while later period drying is due to local African emissions. Asian emissions cause drying in the Gulf of Guinea region via atmospheric circulation adjustments. Notably, there is a weak response to European emission changes in both periods, despite the bulk of North African aerosol burden anomalies being linked to European emissions. In comparing our results with those of Liu et al. (2018), we find that our European and Asian emission responses are similar to the annual mean responses in regional 10x sulfate experiments for CAM5 but differ in sign from the multimodel mean. This suggests there is substantial intermodel uncertainty in the DA effect of regional aerosol emissions on the Sahel. The discrepancy between CAM5 and the rest of the PDRMIP ensemble may be due to the unusually strong aerosol–cloud radiative forcing in the model, as CAM5 was one of two models with prognostic aerosol and both indirect effects in the ensemble (Liu et al. 2018).

As this study uses AGCM simulations, these experiments are idealized and may be affected by errors such as those arising from the lack of ocean–atmosphere coupling, the use of

time-slice rather than transient forcing, and differences in the background SST/SIC state. In the global DA and OM experiments, we find there is statistically significant nonadditivity in the early-period Sahel precipitation response (Fig. 12 in H2020) arising from dependence on the background state. Such background dependence suggests that the response to aerosol forcing may also depend on the level of background GHG forcing (e.g., Deng et al. 2020), although such nonlinearity is not detectable in the CESM1 LE Sahel mean JAS precipitation (H2020). As the GHG concentrations and the background SST are set to 2000s levels, the baseline climate is warmer than the climate in the historical LE experiments, which may change the DA effect due to increased cloud cover and aerosol deposition under warmer conditions (Feichter et al. 2004). It also likely impacts the response to regional perturbations, although we have not tested that here. We find that the sum of the regional perturbation responses often differs substantially from the global perturbation response, even differing in sign in the case of the early-period OM response. However, these differences are not statistically significant due to the noise in each experiment being compounded together when calculating the sum, resulting in large uncertainties. This also means we are not able to assess with confidence the impact of the emission regions we did not include among our DA experiments. Using FDR testing, we assess the statistical robustness of our results and find that the OM responses are quite robust to internal variability in Africa, while the DA responses are less so.

As we find substantial effects of the DA response and remote effects of Pacific and Indian Ocean SST on Sahel precipitation, the effect of aerosol forcing on the Sahel in a coupled system therefore cannot be simply interpreted as a response to the Atlantic hemispheric SST differential. Furthermore, the fact that many of the regional perturbation results change sign and magnitude between the two periods underscores the need to consider the transient response when assessing the aerosol influence on historical climate (and motivates the use of large ensembles, which allow the confident assessment of forced signals on multidecadal time scales; Deser et al. 2020). Thus, care should be taken when interpreting correlations between forced signals in coupled system, as they may covary simply due to their shared forcing and proximate drivers are modulated by remote effects.

Acknowledgments. We thank the reviewers for their constructive comments on this paper. This work was supported by funding from Environment and Climate Change Canada and the National Science and Engineering Research Council of Canada. Computations were performed on the Niagara supercomputer at the SciNet HPC Consortium. SciNet is funded by the Canada Foundation for Innovation; the Government of Ontario; Ontario Research Fund—Research Excellence; and the University of Toronto. This material is based in part on work supported by the National Center for Atmospheric Research (NCAR), which is a major facility sponsored by the National Science Foundation (NSF) under

Cooperative Agreement 1852977. The CESM project is supported primarily by the NSF.

Data availability statement. CESM1 LE data are available from the NCAR Climate Data Gateway (<http://www.cesm.ucar.edu/projects/community-projects/LENS/data-sets.html>). The data used for the results shown in this work can be online (<https://doi.org/10.5683/SP3/1ZGHXA>; Hirasawa et al. 2021).

REFERENCES

- Ackerley, D., B. B. Booth, S. H. E. Knight, E. J. Highwood, D. J. Frame, M. R. Allen, and D. P. Rowell, 2011: Sensitivity of twentieth-century Sahel rainfall to sulfate aerosol and CO₂ forcing. *J. Climate*, **24**, 4999–5014, <https://doi.org/10.1175/JCLI-D-11-00019.1>.
- Andrews, T., P. M. Forster, O. Boucher, N. Bellouin, and A. Jones, 2010: Precipitation, radiative forcing and global temperature change. *Geophys. Res. Lett.*, **37**, L14701, <https://doi.org/10.1029/2010GL043991>.
- Biasutti, M., 2013: Forced Sahel rainfall trends in the CMIP5 archive. *J. Geophys. Res. Atmos.*, **118**, 1613–1623, <https://doi.org/10.1002/jgrd.50206>.
- , 2019: Rainfall trends in the African Sahel: Characteristics, processes, and causes. *Wiley Interdiscip. Rev.: Climate Change*, **10**, e591, <https://doi.org/10.1002/wcc.591>.
- , I. M. Held, A. H. Sobel, and A. Giannini, 2008: SST forcings and Sahel rainfall variability in simulations of the twentieth and twenty-first centuries. *J. Climate*, **21**, 3471–3486, <https://doi.org/10.1175/2007JCLI1896.1>.
- Charney, J. G., 1975: Dynamics of deserts and drought in the Sahel. *Quart. J. Roy. Meteor. Soc.*, **101**, 193–202, <https://doi.org/10.1002/qj.49710142802>.
- Chou, C., and J. D. Neelin, 2004: Mechanisms of global warming impacts on regional tropical precipitation. *J. Climate*, **17**, 2688–2701, [https://doi.org/10.1175/1520-0442\(2004\)017<2688:MOGWIO>2.0.CO;2](https://doi.org/10.1175/1520-0442(2004)017<2688:MOGWIO>2.0.CO;2).
- Chung, C. E., and V. Ramanathan, 2006: Weakening of north Indian SST gradients and the monsoon rainfall in India and the Sahel. *J. Climate*, **19**, 2036–2045, <https://doi.org/10.1175/JCLI3820.1>.
- Deng, J., A. Dai, and H. Xu, 2020: Nonlinear climate responses to increasing CO₂ and anthropogenic aerosols simulated by CESM1. *J. Climate*, **33**, 281–301, <https://doi.org/10.1175/JCLI-D-19-0195.1>.
- Deser, C., A. S. Phillips, I. R. Simpson, N. Rosenbloom, D. Coleman, and S. Stevenson, 2020: Isolating the evolving contributions of anthropogenic aerosols and greenhouse gases: A new CESM1 large ensemble community resource. *J. Climate*, **33**, 7835–7858, <https://doi.org/10.1175/JCLI-D-20-0123.1>.
- Dong, B., and R. Sutton, 2015: Dominant role of greenhouse-gas forcing in the recovery of Sahel rainfall. *Nat. Climate Change*, **5**, 757–760, <https://doi.org/10.1038/nclimate2664>.
- , —, E. Highwood, and L. Wilcox, 2014: The impacts of European and Asian anthropogenic sulfur dioxide emissions on Sahel rainfall. *J. Climate*, **27**, 7000–7017, <https://doi.org/10.1175/JCLI-D-13-00769.1>.
- Dyer, E. L. E., D. B. A. Jones, R. Li, H. Sawaoka, and L. Mudryk, 2017: Sahel precipitation and regional teleconnections with the Indian Ocean. *J. Geophys. Res. Atmos.*, **122**, 5654–5676, <https://doi.org/10.1002/2016JD026014>.

- Feichter, J., E. Roeckner, U. Lohmann, and B. Liepert, 2004: Nonlinear aspects of the climate response to greenhouse gas and aerosol forcing. *J. Climate*, **17**, 2384–2398, [https://doi.org/10.1175/1520-0442\(2004\)017<2384:NAOTCR>2.0.CO;2](https://doi.org/10.1175/1520-0442(2004)017<2384:NAOTCR>2.0.CO;2).
- Folland, C. K., T. N. Palmer, and D. E. Parker, 1986: Sahel rainfall and worldwide sea temperatures, 1901–85. *Nature*, **320**, 602–607, <https://doi.org/10.1038/320602a0>.
- Gaetani, M., G. Messori, Q. Zhang, C. Flamant, and F. S. R. Pausata, 2017: Understanding the mechanisms behind the northward extension of the West African monsoon during the mid-Holocene. *J. Climate*, **30**, 7621–7642, <https://doi.org/10.1175/JCLI-D-16-0299.1>.
- Giannini, A., and A. Kaplan, 2019: The role of aerosols and greenhouse gases in Sahel drought and recovery. *Climatic Change*, **152**, 449–466, <https://doi.org/10.1007/s10584-018-2341-9>.
- , M. Biasutti, I. M. Held, and A. H. Sobel, 2008: A global perspective on African climate. *Climatic Change*, **90**, 359–383, <https://doi.org/10.1007/s10584-008-9396-y>.
- , S. Salack, T. Lodoun, A. Ali, A. T. Gaye, and O. Ndiaye, 2013: A unifying view of climate change in the Sahel linking intra-seasonal, interannual and longer time scales. *Environ. Res. Lett.*, **8**, 024010, <https://doi.org/10.1088/1748-9326/8/2/024010>.
- Gill, A. E., 1980: Some simple solutions for heat-induced tropical circulation. *Quart. J. Roy. Meteor. Soc.*, **106**, 447–462, <https://doi.org/10.1002/qj.49710644905>.
- Held, I. M., T. L. Delworth, J. Lu, K. L. Findell, and T. R. Knutson, 2005: Simulation of Sahel drought in the 20th and 21st centuries. *Proc. Natl. Acad. Sci. USA*, **102**, 17 891–17 896, <https://doi.org/10.1073/pnas.0509057102>.
- Herman, R. J., A. Giannini, M. Biasutti, and Y. Kushnir, 2020: The effects of anthropogenic and volcanic aerosols and greenhouse gases on twentieth century Sahel precipitation. *Sci. Rep.*, **10**, 12203, <https://doi.org/10.1038/s41598-020-68356-w>.
- Hirasawa, H., P. J. Kushner, M. Sigmond, J. Fyfe, and C. Deser, 2020: Anthropogenic aerosols dominate forced multidecadal Sahel precipitation change through distinct atmospheric and oceanic drivers. *J. Climate*, **33**, 10 187–10 204, <https://doi.org/10.1175/JCLI-D-19-0829.1>.
- , —, —, and —, 2021: Data for “Evolving Sahel rainfall response to anthropogenic aerosols driven by shifting regional oceanic and emission influences.” Scholars Portal Dataverse, <https://doi.org/10.5683/SP3/1ZGHXA>.
- Hua, W., A. Dai, L. Zhou, M. Qin, and H. Chen, 2019: An externally forced decadal rainfall seesaw pattern over the Sahel and southeast Amazon. *Geophys. Res. Lett.*, **46**, 923–932, <https://doi.org/10.1029/2018GL081406>.
- Hurrell, J. W., J. J. Hack, D. Shea, J. M. Caron, and J. Rosinski, 2008: A new sea surface temperature and sea ice boundary dataset for the Community Atmosphere Model. *J. Climate*, **21**, 5145–5153, <https://doi.org/10.1175/2008JCLI2292.1>.
- Hwang, Y. T., D. M. W. Frierson, and S. M. Kang, 2013: Anthropogenic sulfate aerosol and the southward shift of tropical precipitation in the late 20th century. *Geophys. Res. Lett.*, **40**, 2845–2850, <https://doi.org/10.1002/grl.50502>.
- Kang, S. M., S. Xie, C. Deser, and B. Xiang, 2021: Zonal mean and shift modes of historical climate response to evolving aerosol distribution. *Sci. Bull.*, **66**, 2405–2411, <https://doi.org/10.1016/j.scib.2021.07.013>.
- Kawase, H., M. Abe, Y. Yamada, T. Takemura, T. Yokohata, and T. Nozawa, 2010: Physical mechanism of long-term drying trend over tropical North Africa. *Geophys. Res. Lett.*, **37**, L09706, <https://doi.org/10.1029/2010GL043038>.
- Liu, L., and Coauthors, 2018: A PDRMIP multimodel study on the impacts of regional aerosol forcings on global and regional precipitation. *J. Climate*, **31**, 4429–4447, <https://doi.org/10.1175/JCLI-D-17-0439.1>.
- Liu, X., and Coauthors, 2012: Toward a minimal representation of aerosols in climate models: Description and evaluation in the Community Atmosphere Model CAM5. *Geosci. Model Dev.*, **5**, 709–739, <https://doi.org/10.5194/gmd-5-709-2012>.
- Lu, J., 2009: The dynamics of the Indian Ocean sea surface temperature forcing of Sahel drought. *Climate Dyn.*, **33**, 445–460, <https://doi.org/10.1007/s00382-009-0596-6>.
- Malavelle, F. F., and Coauthors, 2017: Strong constraints on aerosol–cloud interactions from volcanic eruptions. *Nature*, **546**, 485–491, <https://doi.org/10.1038/nature22974>.
- Mohino, E., S. Janicot, and J. Bader, 2011: Sahel rainfall and decadal to multi-decadal sea surface temperature variability. *Climate Dyn.*, **37**, 419–440, <https://doi.org/10.1007/s00382-010-0867-2>.
- Myhre, G., and Coauthors, 2017: PDRMIP: A Precipitation Driver and Response Model Intercomparison Project—Protocol and preliminary results. *Bull. Amer. Meteor. Soc.*, **98**, 1185–1198, <https://doi.org/10.1175/BAMS-D-16-0019.1>.
- Neale, R. B., and Coauthors, 2012: Description of the NCAR Community Atmosphere Model (CAM 5.0). NCAR Tech. Note NCAR/TN-486+STR, 274 pp., www.cesm.ucar.edu/models/cesm1.0/cam/docs/description/cam5_desc.pdf.
- Pausata, F. S. R., G. Messori, and Q. Zhang, 2016: Impacts of dust reduction on the northward expansion of the African monsoon during the Green Sahara period. *Earth Planet. Sci. Lett.*, **434**, 298–307, <https://doi.org/10.1016/j.epsl.2015.11.049>.
- Privé, N. C., and A. R. Plumb, 2007: Monsoon dynamics with interactive forcing. Part I: Axisymmetric studies. *J. Atmos. Sci.*, **64**, 1417–1430, <https://doi.org/10.1175/JAS3916.1>.
- Rodríguez-Fonseca, B., and Coauthors, 2011: Interannual and decadal SST-forced responses of the West African monsoon. *Atmos. Sci. Lett.*, **12**, 67–74, <https://doi.org/10.1002/asl.308>.
- Rotstayn, L. D., and U. Lohmann, 2002: Tropical rainfall trends and the indirect aerosol effect. *J. Climate*, **15**, 2103–2116, [https://doi.org/10.1175/1520-0442\(2002\)015<2103:TRTATI>2.0.CO;2](https://doi.org/10.1175/1520-0442(2002)015<2103:TRTATI>2.0.CO;2).
- Rowell, D. P., 2001: Teleconnections between the tropical Pacific and the Sahel. *Quart. J. Roy. Meteor. Soc.*, **127**, 1683–1706, <https://doi.org/10.1002/qj.49712757512>.
- Samset, B. H., and Coauthors, 2016: Fast and slow precipitation responses to individual climate forcers: A PDRMIP multimodel study. *Geophys. Res. Lett.*, **43**, 2782–2791, <https://doi.org/10.1002/2016GL068064>.
- Smith, S. J., J. van Aardenne, Z. Klimont, R. J. Andres, A. Volke, and S. Delgado Arias, 2011: Anthropogenic sulfur dioxide emissions: 1850–2005. *Atmos. Chem. Phys.*, **11**, 1101–1116, <https://doi.org/10.5194/acp-11-1101-2011>.
- Toll, V., M. Christensen, J. Quaas, and N. Bellouin, 2019: Weak average liquid-cloud-water response to anthropogenic aerosols. *Nature*, **572**, 51–55, <https://doi.org/10.1038/s41586-019-1423-9>.
- Undorf, S., M. A. Bolasina, and G. C. Hegerl, 2018: Impacts of the 1900–74 increase in anthropogenic aerosol emissions from North America and Europe on Eurasian summer climate. *J. Climate*, **31**, 8381–8399, <https://doi.org/10.1175/JCLI-D-17-0850.1>.
- Wang, C., 2015: Anthropogenic aerosols and the distribution of past large-scale precipitation change. *Geophys. Res. Lett.*, **42**, 10 876–10 884, <https://doi.org/10.1002/2015GL066416>.

- Westervelt, D. M., and Coauthors, 2017: Multimodel precipitation responses to removal of U.S. sulfur dioxide emissions. *J. Geophys. Res. Atmos.*, **122**, 5024–5038, <https://doi.org/10.1002/2017JD026756>.
- Wilks, D. S., 2016: “The stippling shows statistically significant grid points”: How research results are routinely overstated and overinterpreted, and what to do about it. *Bull. Amer. Meteor. Soc.*, **97**, 2263–2273, <https://doi.org/10.1175/BAMS-D-15-00267.1>.
- Zelinka, M. D., T. Andrews, P. M. Forster, and K. E. Taylor, 2014: Quantifying components of aerosol–cloud–radiation interactions in climate models. *J. Geophys. Res. Atmos.*, **119**, 7599–7615, <https://doi.org/10.1002/2014JD021710>.